J. Appl. Environ. Biol. Sci., 4(2)271-283, 2014

© 2014, TextRoad Publication

ISSN: 2090-4274
Journal of Applied Environmental and Biological Sciences
www.textroad.com

Strain Localization Simulation in Plane-Strain Biaxial Tests on Dense Hostun RF Sand Using Mixed XFEM and Integral Type Nonlocal Model

Zarinfar Meysam, Kalantary Farzin

Civil Engineering Department, K.N.Toosi University of Technology, Tehran, Iran

Received: November 3 2013
Accepted: December 8 2013

ABSTRACT

Strain-softening causes localization of the strain which is accompanied by an instantaneous vanishing of the stress. If the modeling approach for strain localization with softening does not contain a material length-scale parameter, the numerical simulation suffers from the excessive mesh dependence. The nonlocal continuum concept has emerged as an effective means for regularizing the boundary value problems with strain softening. In this paper, the calculations were carried out with integral type nonlocal constitutive law to model properly the shear zone formation. For nonlocal plasticity, element size had a critical effect on the solution. Sufficiently refined meshes were required for an accurate solution without mesh dependency. The XFEM method was employed for simulation of high strain gradient in the localization band. It was shown that an extended finite element method can be applied to the problem to decrease the required mesh density close to the localization band. A new method based on the local bifurcation theory was proposed for the initiation and growth criterion of the strain localization interface. In the case of non associated constitutive model, the criterion for bifurcation was reduced to the singularity of the symmetric part of the acoustic tensor. Finally, the ability of the presented model to describe the behavior of granular materials was demonstrated by comparisons of the results of numerical calculations and drained biaxial tests on dense Hostun sand. Attention was laid on the effect of the regularization technique on the load–displacement curve and shear zone orientation. The calculated load–displacement curves coincided very well with experiment. In addition, the influence of mean effective stress was investigated. It was shown that when increasing the confining stress, the onset of strain localization was delayed. Shear band orientation were obtained similarly to those observed experimentally. The contours of symmetric part of the acoustic tensor indicated that shear banding initiated at, or shortly before peak.

KEYWORDS: XFEM, Nonlocal plasticity, Shear band localization, Shear band orientation, Mean effective stress, Biaxial tests, Dense sand

1- INTRODUCTION

Strain localization refers to the localization of deformation into thin zones of intense shearing. It has been realized that strain localization affects bearing capacity of structures. Strain localization is often treated as strain softening in continuum mechanics. It was mentioned in the literature that classical continuum mechanics cannot correctly predict strain localization and softening behavior. Strain softening, when incorporated in a computational model, exhibits undesirable characteristics. So, reliable predictions of the bearing capacity are not possible in the framework of classical or local continuum theory. When localization or material softening occurs, the governing static equations lose ellipticity or the governing dynamic equations lose hyperbolicity (onset of bifurcation) [1, 2]. Loss of ellipticity corresponds to a situation in which either the number of linearly independent solutions to the equilibrium equations is infinite and (or) these solutions do not depend continuously on the data [3]. Therefore, the initial value problem becomes mathematically ill-posed. This implies a strong dependence of the shear band width on the spatial discretization. This inefficiency is due to the fact that classical continuum mechanics has no material length scale parameter [4]. As a result, by refining the mesh, the plastic strain is localized in a narrower region. To overcome this unphysical behavior, micro-polar models [5], higher-order gradient models [6], visco-plasticity [7] and integral-type nonlocal plasticity models [8, 9] are commonly used.

The approach used here is the mixed XFEM and integral type nonlocal model which is based on the assumption that stress at a point is determined not only by the current values and the previous history of deformation at that point but also by the state of its neighboring points. The first application of the integral-

Corresponding author: Zarinfar Meysam, Civil Engineering Department, K.N.Toosi University of Technology.
Tel: +989183521041; Fax: +982188779476; Email address: zarinfar@dena.kntu.ac.ir

type nonlocal model into plasticity was made by Eringen [10, 11]. Pijaudier-Cabot and Bazant [12] and Bazant and Lin [13] applied the nonlocal operator only to those parameters which control the softening process. Finite element implementation of nonlocal plasticity was presented by Stromberg and Ristinmaa [14], Brunig et al. [15], Maier [16, 17] and Tejchman [18]. Jirasek [19] presented an overview of the integral-type nonlocal model for damage and fracture, Bazant and Jirasek [20] did for plasticity and damage, and Jirasek and Rolshoven [4] did for plasticity. The mathematical foundation of the XFEM was discussed by Melenk and Babuska [21]. The first application of XFEM to crack growth problems was done by Belytschko and Black [22]. The advantage of this technique is its independency of the crack geometry on the mesh. Fries and Belytschko [23] provided an overview of XFEM applications. This numerical technique has been used to simulate shear bands and strain localization [24-29].

The objective of this paper is to investigate and provide insight into the localization phenomenon in dense sand under fully drained conditions. Most of the literature about nonlocal models deals with their mechanical and numerical implementation. But in order to judge the ability of a model to describe the mechanical behavior of a material comparisons of numerical calculations with results of laboratory tests are necessary. These are very rarely found in literature. The results of biaxial tests on dense Hostun RF sand [30, 31] are predicted and so the ability of the proposed model to describe the mechanical behavior of granular materials demonstrated. The analysis is performed with extended finite element method on the basis of the integral type nonlocal model. During calculations, the emphasis is placed on the orientation of the localization zone, the effect of the mean stress and the evolution of localization band.

It is well known that dense sand, especially when tested in plane strain condition, show early strain localization, with severe overall strength reduction immediately after the onset of localization. In the present paper, a new method based on the local bifurcation theory is proposed for the initiation and growth criterion of the strain localization interface. Strain localization starts when the ellipticity conditions of the static equation or the hyperbolicity of the dynamic equation are lost (onset of bifurcation) [13, 32]. In the case of non associated constitutive model, this condition is equivalent to zero or the negative determinant of the symmetric part of the acoustic tensor. Zarinfar and Kalantary [9] proposed the similar numerical algorithm for associated constitutive model. Therefore, the singularity of the symmetric part of the acoustic tensor was considered as the onset condition of strain localization (local bifurcation criterion) [33-37]. When using the local bifurcation theory and XFEM, the softening zone initiation locus does not need to be known in advance. Strain localization begins at the first point in which the local criterion of bifurcation is satisfied (singularity of acoustic tensor). Moreover, the strain localization interface progresses are obtained independently from the mesh. With continued loading, local criterion of bifurcation is satisfied in more points and thereafter strain localization grows inside the body.

In summery, the scientific contributions of this paper are 1) a new method based on the local bifurcation theory is proposed for the initiation and growth criterion of the strain localization interface for non associated constitutive model 2) nonlocal theory is combined with XFEM for reduction of computational effort and mesh dependency 3) the localization phenomenon in dense sand under fully drained conditions is investigated.

The paper is organized as follows: first in section 2, integral type nonlocal is briefly recalled, in section 3, governing equations are briefly recalled and XFEM is applied to the governing equations, in section 4, a new method for the initiation and growth criterion of the strain localization interface is discussed, Finally, in section 5, the performance of the nonlocal formulation and mixed nonlocal-XFEM formulation are compared and the results of biaxial tests on dense Hostun RF sand are predicted to demonstrate the efficiency of the proposed model in shear band localization modeling without mesh dependency.

2. Integral type nonlocal model

Nonlocal continuum theory uses integral averaging of the variable around its neighborhood, instead of a local definition. For example, nonlocal averaging of plastic strain tensor ($\bar{\varepsilon}_{ij}^{p}$) at location x may be defined by the local plastic strain tensor (ε_{ij}^{p}).

$$\bar{\varepsilon}_{ij}^{p}(\mathbf{x}) = \int_V \alpha'(\mathbf{x},\boldsymbol{\xi})\varepsilon_{ij}^{p}(\boldsymbol{\xi})dV \tag{1}$$

where V denotes volume of the body, $\alpha'(\mathbf{x},\boldsymbol{\xi})$ is suitable weighting function. In this paper Gaussian distribution function is used as a weighting function.

$$\alpha'(\mathbf{x},\xi)=\frac{e^{-\left(2|\xi-\mathbf{x}|/\gamma\right)^2}}{\int_V e^{-\left(2|\zeta-\mathbf{x}|/\gamma\right)^2}dV} \tag{2}$$

in which γ is a scalar which is related to material length scale parameter. For numerical finite element computation, nonlocal plastic strain tensor can be written as follow:

$$\bar{\varepsilon}_{ij}^{p}(\mathbf{x})=\sum_{k}\alpha'(\mathbf{x},\mathbf{x}_k)\varepsilon_{ij}^{p}(\mathbf{x}_k) \tag{3}$$

where k denotes gauss points which are closer to point $\mathbf{x}$ than 2γ. The value of $\alpha'(\mathbf{x},\xi)$ for gauss points with greater distance than 2γ is negligible.

In this paper, equation 4 is used to calculate the effective stress vector.

$$\dot{\boldsymbol{\sigma}}=\mathbf{D^e}\dot{\boldsymbol{\varepsilon}}-(1-m)\mathbf{D^e}\dot{\boldsymbol{\varepsilon}}^{\mathbf{p}}-m\mathbf{D^e}\dot{\bar{\boldsymbol{\varepsilon}}}^{\mathbf{p}} \tag{4}$$

where $\mathbf{D}^e$ is linear elastic matrix and m is a constant parameter. Using equation 4, the stress rate at a certain point is related to the plastic strain rate in its neighborhood. The formulation presented by Bazant and Lin [13] is a special case of equation 4 where m is considered to be 1. Local plastic strain rate is obtained by equation 5.

$$\dot{\boldsymbol{\varepsilon}}^{\mathbf{p}}=\dot{\lambda}\frac{\partial F}{\partial\boldsymbol{\sigma}} \tag{5}$$

where $\dot{\lambda}$ denotes the plastic multiplier and F the yield function which can be defined as: $F(\boldsymbol{\sigma},\kappa)=f(\boldsymbol{\sigma})-\kappa=0$ in which κ is the hardening-softening parameter. Applying the consistency condition to the yield function, $\dot{\boldsymbol{\varepsilon}}^{\mathrm{p}}$ can be calculated as:

$$\dot{\boldsymbol{\varepsilon}}^{\mathrm{p}}=\frac{\partial F/\partial\boldsymbol{\sigma}\left(\partial F/\partial\boldsymbol{\sigma}\right)^{\mathrm{T}}\mathbf{D^e}}{\mathrm{H}+\left(\partial F/\partial\boldsymbol{\sigma}\right)^{\mathrm{T}}\mathbf{D^e}\left(\partial F/\partial\boldsymbol{\sigma}\right)}\dot{\boldsymbol{\varepsilon}}=\Lambda\dot{\boldsymbol{\varepsilon}} \tag{6}$$

where H denotes the plastic tangential modulus and is equal to $-(\partial F/\partial\kappa)(\partial\kappa/\partial\boldsymbol{\varepsilon}^{p})$. Finally, stress rate at gauss point k can be defined by:

$$\dot{\boldsymbol{\sigma}}_k=\mathbf{D}_k^{\mathrm{e}}\left(\mathbf{I}-(1-\mathrm{m})\boldsymbol{\Lambda}_k\right)\dot{\boldsymbol{\varepsilon}}_k-\mathrm{m}\mathbf{D}_k^{\mathrm{e}}\left(\sum_{l}\boldsymbol{\Lambda}_l\,\alpha'(\mathbf{x}_k,\mathbf{x}_l)\dot{\boldsymbol{\varepsilon}}_l\right) \tag{7}$$

where $\mathbf{I}$ is identity matrix and l denotes gauss points which are closer to gauss point k than 2γ.

2. Integral type nonlocal model enhanced by XFEM

XFEM improves the description of the displacement field inside the localized zone by adding the special enrichment functions which can model high gradient of displacement field. These functions and their gradients must be similar to the profile of displacement and strain fields. The approximation of displacement ($\mathbf{u}$) can be expressed as follow:

$$\mathbf{u}_{(\mathbf{x},t)}=\sum_{i=1}^{n_{nod}^{u}}N_{i(\mathbf{x})}^{u}\bar{\mathbf{u}}_{i(t)}+\sum_{i=1}^{n_{nod}^{u}}N_{i(\mathbf{x})}^{u}\left(R_{(\mathbf{x})}[\psi_{(\varphi(\mathbf{x}))}-\bar{\psi}_{(\varphi(\mathbf{x}_i))}]\bar{\mathbf{a}}_{i(t)}\right)=\sum_{i=1}^{n_{nod}^{u}}N_{i(\mathbf{x})}^{u}\bar{\mathbf{u}}_{i(t)}+\sum_{i=1}^{n_{nod}^{u}}N_{i(\mathbf{x})Enr}^{u}\bar{\mathbf{a}}_{i(t)} \tag{8}$$

where n_{nod}^{u} denotes the number of element nodes, N_i^u the standard finite element shape function associated with node i, $\bar{\mathbf{u}}_i$ the standard nodal displacement, $\bar{\mathbf{a}}_i$ the additional degrees of freedom (DOF) associated with node i. In the above relation, $\psi_{(\mathbf{x})}$ denotes the appropriate enrichment function and $\varphi(\mathbf{x})$ is the distance from the strain localization interface. $R_{(\mathbf{x})}$ is the ramp function which resolves difficulties in blending elements [23]. In this study, the hyperbolic tangent is employed to describe the corresponding profiles. This function is defined as:

$$\psi_{\varphi(x)}=tanh\left(2\varphi(\mathbf{x})/\beta\right) \tag{9}$$

where β is the parameter which controls width of the shear band. By selecting several values of β, one can construct a series of enrichment functions describing the displacement profile near the strain localization interface. By substituting equation (8) in to strain rate definition, strain matrix can be defined as:

$$\dot{\boldsymbol{\varepsilon}}=\sum_{i=1}^{n_{nod}^{u}}\begin{bmatrix}\mathbf{B}_{i(\mathbf{x})} & \mathbf{B}_{i(\mathbf{x})Enr}\end{bmatrix}\begin{bmatrix}\dot{\bar{\mathbf{u}}}_{i(t)}\\ \dot{\bar{\mathbf{a}}}_{i(t)}\end{bmatrix} \tag{10}$$

in which

$$\mathbf{B}_{i(\mathbf{x})}=\begin{bmatrix}\dfrac{\partial N^u_{i(\mathbf{x})}}{\partial x_1} & 0\\ 0 & \dfrac{\partial N^u_{i(\mathbf{x})}}{\partial x_2}\\ \dfrac{\partial N^u_{i(\mathbf{x})}}{\partial x_2} & \dfrac{\partial N^u_{i(\mathbf{x})}}{\partial x_1}\end{bmatrix}\quad \mathbf{B}_{i(x)Enr}=\begin{bmatrix}\dfrac{\partial N^u_{i(\mathbf{x})Enr}}{\partial x_1} & 0\\ 0 & \dfrac{\partial N^u_{i(\mathbf{x})Enr}}{\partial x_2}\\ \dfrac{\partial N^u_{i(\mathbf{x})Enr}}{\partial x_2} & \dfrac{\partial N^u_{i(\mathbf{x})Enr}}{\partial x_1}\end{bmatrix} \tag{11}$$

The governing equation in an updated Lagrangian framework is a linear momentum balance equation.

$$\mathrm{div}\boldsymbol{\sigma}-\rho\ddot{\mathbf{u}}+\rho\mathbf{b}=0 \tag{12}$$

where $\boldsymbol{\sigma}$ is the stress, $\mathbf{b}$ refers to the body force and ρ is the density. The Dirichlet boundary condition is $\mathbf{u}=\bar{\mathbf{u}}$ on $\Gamma=\Gamma_{\mathbf{u}}$. The Neumann boundary conditions is $\mathbf{t}=\boldsymbol{\sigma}\mathbf{n}=\bar{\mathbf{t}}$ on $\Gamma=\Gamma_{\mathbf{t}}$. To obtain the weak form of the governing equations, Galerkin's procedure is used. The test functions $\delta\square\mathbf{u}(\mathbf{x},t)$ which has the same form as $\mathbf{u}$ is multiplied by equations (12) and integrated over the domain $\boldsymbol{\Omega}$. Using the Divergence theorem leads to the following equation as:

$$\mathbf{M}\begin{bmatrix}\ddot{\mathbf{u}}\\ \ddot{\mathbf{a}}\end{bmatrix}+\int_\Omega \mathbf{B}^{\mathbf{T}}\boldsymbol{\sigma}\mathrm{d}\Omega-\mathbf{F}=0 \tag{13}$$

in which

$$\mathbf{M}=\begin{bmatrix}\int_\Omega(\mathbf{N}^{\mathbf{u}})^{\mathrm{T}}\rho\mathbf{N}^{\mathbf{u}}\mathrm{d}\Omega & \int_\Omega(\mathbf{N}^{\mathbf{u}})^{\mathrm{T}}\rho\mathbf{N}^{\mathbf{u}}_{Enr}\mathrm{d}\Omega\\ \int_\Omega(\mathbf{N}^{\mathbf{u}}_{Enr})^{\mathrm{T}}\rho\mathbf{N}^{\mathbf{u}}\mathrm{d}\Omega & \int_\Omega(\mathbf{N}^{\mathbf{u}}_{Enr})^{\mathrm{T}}\rho\mathbf{N}^{\mathbf{u}}_{Enr}\mathrm{d}\Omega\end{bmatrix} \tag{14}$$

$$\mathbf{F}=\begin{bmatrix}\int_\Omega(\mathbf{N}^{\mathbf{u}})^{\mathrm{T}}\rho\mathbf{b}\mathrm{d}\Omega+\int_{\Gamma_t}(\mathbf{N}^{\mathbf{u}})^{\mathrm{T}}\bar{\mathbf{t}}\mathrm{d}\Gamma\\ \int_\Omega(\mathbf{N}^{\mathbf{u}}_{Enr})^{\mathrm{T}}\rho\mathbf{b}\mathrm{d}\Omega+\int_{\Gamma_t}(\mathbf{N}^{\mathbf{u}}_{Enr})^{\mathrm{T}}\bar{\mathbf{t}}\mathrm{d}\Gamma\end{bmatrix} \tag{15}$$

The governing equations (13) are discretised in the time domain by means of the Newmark's scheme.

$$\left[\mathbf{M}+.5\beta_2\Delta t^2\mathbf{K}\right]\begin{bmatrix}\Delta\ddot{\bar{\mathbf{u}}}^t\\ \Delta\ddot{\bar{\mathbf{a}}}^t\end{bmatrix}=\left[-\boldsymbol{\Psi}\right] \tag{16}$$

In above equation, $\boldsymbol{\Psi}$ denotes the vector of known values at time t and $\mathbf{K}$ is the tangential stiffness matrix.

$$\boldsymbol{\Psi}=\mathbf{M}\begin{bmatrix}\ddot{\bar{\mathbf{u}}}^{\mathrm{t}}\\ \ddot{\bar{\mathbf{a}}}^{\mathrm{t}}\end{bmatrix}+\mathbf{K}\begin{bmatrix}\bar{\mathbf{u}}^{\mathrm{t}}+\dot{\bar{\mathbf{u}}}^{\mathrm{t}}\Delta t+.5\ddot{\bar{\mathbf{u}}}^{\mathrm{t}}\Delta t^2\\ \bar{\mathbf{a}}^{\mathrm{t}}+\dot{\bar{\mathbf{a}}}^{\mathrm{t}}\Delta t+.5\ddot{\bar{\mathbf{a}}}^{\mathrm{t}}\Delta t^2\end{bmatrix}-(\mathbf{F})^{t+\Delta t} \tag{17}$$

$$\mathbf{K}=\frac{d\left(\int_\Omega \mathbf{B}^{\mathbf{T}}\boldsymbol{\sigma}\mathrm{d}\Omega\right)}{d(\mathbf{u},\mathbf{a})}=\begin{bmatrix}\int_\Omega \mathbf{B}^T\mathbf{D}\ \mathbf{B}\ \mathrm{d}\Omega & \int_\Omega \mathbf{B}^T\mathbf{D}\ \mathbf{B}_{Enr}\mathrm{d}\Omega\\ \int_\Omega \mathbf{B}^T_{Enr}\mathbf{D}\ \mathbf{B}\ \mathrm{d}\Omega & \int_\Omega \mathbf{B}^T_{Enr}\mathbf{D}\ \mathbf{B}_{Enr}\mathrm{d}\Omega\end{bmatrix} \tag{18}$$

where $\mathbf{D}$ is the appropriate constitutive matrix. The non-linear coupled equation system is linearised in a standard way thus yielding the linear algebraic equation system 16 which can be solved using an appropriate approach, such as the Newton-Raphson procedure.

The tangent stiffness matrix for integral type nonlocal plasticity enhanced by XFEM for a specified element can be obtained as follow:

$$\mathbf{K} = \sum_k |J| W_k \begin{bmatrix} \mathbf{B}^{\mathrm{T}}_{(\mathrm{x_k})}\mathbf{D}^{\mathrm{e}}_{\mathrm{k}}(\mathrm{I}-\mathbf{\Lambda}_{\mathrm{k}})\mathbf{B}_{(\mathrm{x_k})} & \mathbf{B}^{\mathrm{T}}_{(\mathrm{x_k})}\mathbf{D}^{\mathrm{e}}_{\mathrm{k}}(\mathrm{I}-\mathbf{\Lambda}_{\mathrm{k}})\mathbf{B}_{(\mathrm{x_k})\mathrm{Enr}} \\ \mathbf{B}^{\mathrm{T}}_{(\mathrm{x_k})\mathrm{Enr}}\mathbf{D}^{\mathrm{e}}_{\mathrm{k}}(\mathrm{I}-\mathbf{\Lambda}_{\mathrm{k}})\mathbf{B}_{(\mathrm{x_k})} & \mathbf{B}^{\mathrm{T}}_{(\mathrm{x_k})\mathrm{Enr}}\mathbf{D}^{\mathrm{e}}_{\mathrm{k}}(\mathrm{I}-\mathbf{\Lambda}_{\mathrm{k}})\mathbf{B}_{(\mathrm{x_k})\mathrm{Enr}} \end{bmatrix} + \dots$$

$$\dots + \mathrm{m}\sum_k |J| W_k \begin{bmatrix} \mathbf{B}^{\mathrm{T}}_{(\mathrm{x_k})}\mathbf{D}^{\mathrm{e}}_{\mathrm{k}}(\mathbf{\Lambda}_{\mathrm{k}})\mathbf{B}_{(\mathrm{x_k})} & \mathbf{B}^{\mathrm{T}}_{(\mathrm{x_k})}\mathbf{D}^{\mathrm{e}}_{\mathrm{k}}(\mathbf{\Lambda}_{\mathrm{k}})\mathbf{B}_{(\mathrm{x_k})\mathrm{Enr}} \\ \mathbf{B}^{\mathrm{T}}_{(\mathrm{x_k})\mathrm{Enr}}\mathbf{D}^{\mathrm{e}}_{\mathrm{k}}(\mathbf{\Lambda}_{\mathrm{k}})\mathbf{B}_{(\mathrm{x_k})} & \mathbf{B}^{\mathrm{T}}_{(\mathrm{x_k})\mathrm{Enr}}\mathbf{D}^{\mathrm{e}}_{\mathrm{k}}(\mathbf{\Lambda}_{\mathrm{k}})\mathbf{B}_{(\mathrm{x_k})\mathrm{Enr}} \end{bmatrix} + \dots \tag{19}$$

$$\dots - \mathrm{m}\sum_k\sum_l |J| W_k \begin{bmatrix} \mathbf{B}^{\mathrm{T}}_{(\mathrm{x_k})}\mathbf{D}^{\mathrm{e}}_{\mathrm{k}}(\mathbf{\Lambda}_{\mathrm{k}})\alpha'(\mathbf{x}_{\mathrm{k}},\mathbf{x}_l)\mathbf{B}_{(\mathrm{x_l})} & \mathbf{B}^{\mathrm{T}}_{(\mathrm{x_k})}\mathbf{D}^{\mathrm{e}}_{\mathrm{k}}(\mathbf{\Lambda}_{\mathrm{k}})\alpha'(\mathbf{x}_{\mathrm{k}},\mathbf{x}_l)\mathbf{B}_{(\mathrm{x_l})\mathrm{Enr}} \\ \mathbf{B}^{\mathrm{T}}_{(\mathrm{x_k})\mathrm{Enr}}\mathbf{D}^{\mathrm{e}}_{\mathrm{k}}(\mathbf{\Lambda}_{\mathrm{k}})\alpha'(\mathbf{x}_{\mathrm{k}},\mathbf{x}_l)\mathbf{B}_{(\mathrm{x_l})} & \mathbf{B}^{\mathrm{T}}_{(\mathrm{x_k})\mathrm{Enr}}\mathbf{D}^{\mathrm{e}}_{\mathrm{k}}(\mathbf{\Lambda}_{\mathrm{k}})\alpha'(\mathbf{x}_{\mathrm{k}},\mathbf{x}_{\mathrm{l}})\mathbf{B}_{(\mathrm{x_l})\mathrm{Enr}} \end{bmatrix}$$

where $|J|$ is determinant of Jacobian matrix and W_k denotes weight coefficient of the gaussian quadrature. If the second and third terms in equation 19 are ignored, the formulation becomes equivalent to local theory. The DOF of one element may become related to the DOF of a non-neighboring element because of the third term of equation 19. In conclusion, the nonzero components of the tangent stiffness matrix increase. In this situation, the tangent stiffness matrix is not symmetrical because $\alpha'(\mathbf{x}_k, \mathbf{x}_l) \neq \alpha'(\mathbf{x}_l, \mathbf{x}_k)$.

4. Initiation and growth criterion of the strain localization interface

This study proposed the local bifurcation criterion to locate strain localization interface. Zarinfar and Kalantary [9] proposed the similar numerical algorithm for associated constitutive model. But in the case of a non associated constitutive model, this criterion coincides with the singularity of the symmetric part of the acoustic tensor [2, 35]. Acoustic tensor can be defined as:

$$A_{ij} = C^{ep}_{ikjl} n_k n_l \tag{20}$$

where n is a unit vector and C^{ep}_{ikjl} denotes local elastoplastic constitutive tensor.

$$C^{ep}_{ikjl} = C^{e}_{ikjl} - \frac{C^{e}_{ikmn}\,\partial F/\partial\sigma_{mn} C^{e}_{pqjl}\,\partial F/\partial\sigma_{pq}}{\left(H + \partial F/\partial\sigma_{rs} C^{e}_{rstu}\,\partial F/\partial\sigma_{tu}\right)} \tag{21}$$

If there is a direction in which the determinant of the symmetric part of the acoustic tensor becomes zero or negative, strain localization probably starts, and XFEM must be used to approximate the displacement field. At each Gauss point, then, a direction must be found in which the determinant of the symmetric part of the acoustic tensor has the lowest value. One independent variable is sufficient to describe unit vector n in two-dimensional space. As a result, the determinant is a function of one variable, and its lowest value can easily be calculated. This approach allows us to identify points where strain localization is likely to occur.

In order to perform the numerical algorithm, it is assumed that the interface, i.e. the centerline of the localization zone, and the Gauss points which have a negative determinant of the symmetric part of the acoustic tensor are known at time t (Fig. 1). Moreover, the vector V corresponding to the minimum determinant of the symmetric part of the acoustic tensor at the last point of the interface, i.e. L, is known at time t.

The vector V' is plotted from L to the Gauss point which has a negative determinant, i.e. G. Then the angle between V and V' is obtained. The next point for the centerline of the localization zone is a Gauss point whose corresponding vector V' has a minimum angle with V. Once the new interface is detected, additional DOF are activated at every nodal point whose support has an intersection with the enriched zone. If convergency is obtained at the end of the increment, the evolution of shear band is carried out to obtain the new interface for the next loading step. This technique is simple and has been employed in the examples. To avoid doubling back on the original path, the angle between the pieces of strain localization interface must be less than 90 degrees.

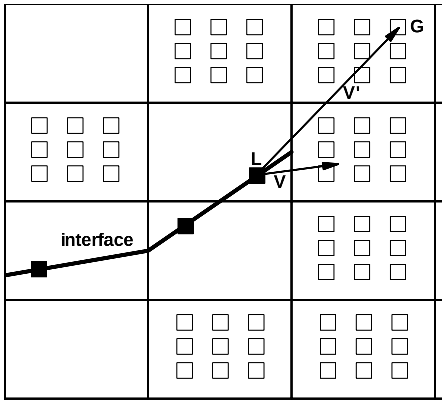

Fig.1 numerical computation for the evolution of localization band at step *n*

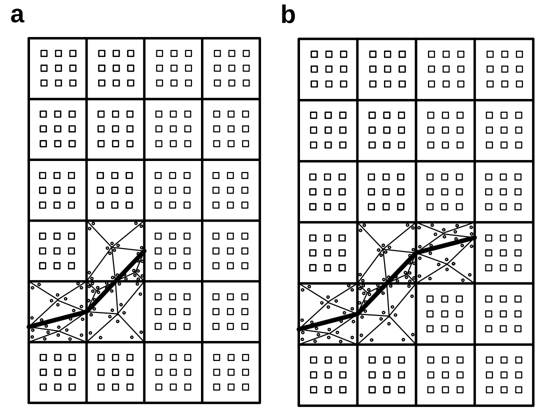

Fig.2 decomposition of the elements into sub-elements at step n and n + 1

5. Numerical simulation

A computer program has been developed to investigate the computational aspects of the XFEM model in a higher order continuum model. The finite element mesh employed in all simulations was eight-noded rectangular plane strain elements with nine integration points. The analysis starts with the standard FE model with no enrichment functions. The enrichment function is then implemented into the standard shape functions by tracing the evolution of shear band zone. The parameter β, which is defined the width of enrichment zone, is set to γ in all analyzes due to the fact that the shear band thickness is about γ. All elements closer to the strain localization interface than β are enriched by the hyperbolic tangent function.

For integration purposes, a decomposition of the elements into sub-elements that align with the interface is standard in the XFEM [23]. In the case of a rectangular element, the elements located on the interface were partitioned using triangular sub-elements (Fig. 2a) and 24 Gauss quadrature points were used for the elements cut by the shear band interface. For standard FE elements, a set of 3×3 Gauss points were used for numerical integration. If an interface surface was added during the evolution of the shear band zone (Fig. 2b), the number of Gauss quadrature points for an element may differ before and after each increment. In this case, the value of the stresses can be determined at the standard FE Gauss points of an element. To obtain these values at the Gauss quadrature points of sub-triangles, a simple interpolation on a support domain for each triangular Gauss point consisting of the three nearest standard FE Gauss points was used. The required stress value can be determined using a simple interpolation.

5.1. Plane strain strip in tension

In this example, the performance of the nonlocal formulation and mixed nonlocal-XFEM formulation were compared. The geometry, boundary conditions and material parameters are shown in Fig. 3. The shaded area in Fig 3 represents the weak inclusion. The parameter γ was set to 1cm and *m* was set to 1.5 to obtain the shear band thickness equal to 1.3 cm. In order to show the capability of the nonlocal extension with XFEM, numerical results obtained using different meshes are presented. The meshes consisted of 96, 384 and 651 four-node.

The results of the nonlocal and mixed XFEM-nonlocal formulation are shown in Fig 4 and 5. These figures present the nonlocal effective plastic strain contours for both formulations. As seen in Fig 4, the results for coarse mesh are different than for other mesh results in the nonlocal formulation. In the proposed approach, good agreement can be observed between the three mesh sizes; therefore, the XFEM can be applied to the problem to decrease the required mesh density close to the of the localization band. These figures confirm that mixed XFEM-nonlocal technique gives good prediction of localization even for the coarse mesh. As seen, there is a good agreement between the results of the proposed approach for different meshes i.e. the width and inclination of the shear band are independent of the element size.

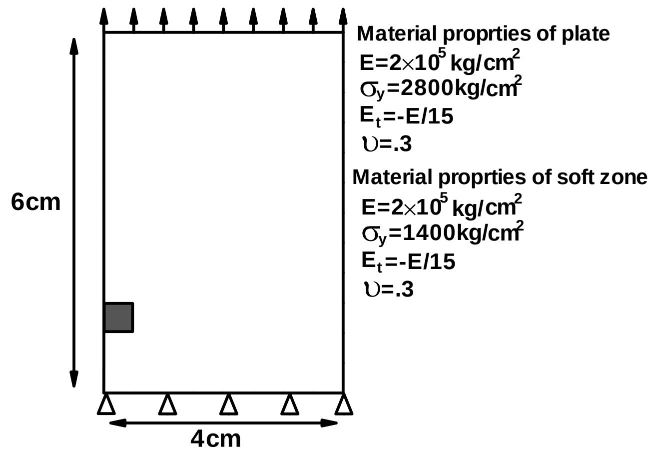

Fig.3 The plane strain strip in tension; the geometry, boundary conditions, and material properties

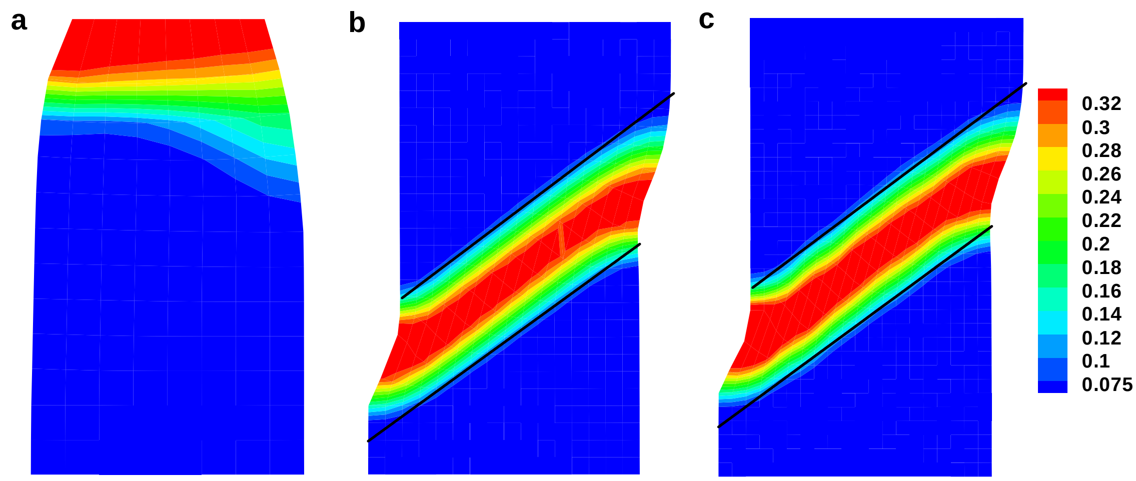

Fig.4 the nonlocal effective plastic strain contours for nonlocal model; a) coarse mesh b)medium mesh c) fine mesh

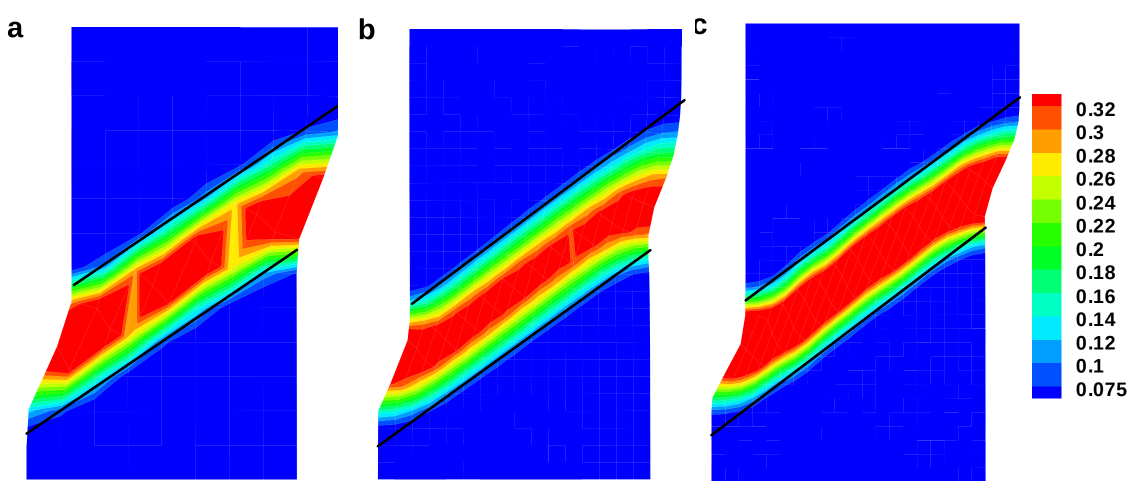

Fig.5 the nonlocal effective plastic strain contours for mixed XFEM-nonlocal model; a) coarse mesh b) medium mesh c) fine mesh

5.3. Simulation of plane strain biaxial tests on dense Hostun RF sand

In the following the results of plane strain biaxial tests on dense Hostun RF sand performed by Desrues and Hammad [30] will be compared with numerical calculations done with the integral type nonlocal model enhanced by XFEM. Numerical calculations of plane strain compression tests were performed with a specimen which was 34 cm high and 10 cm wide. The stress–strain curve, geometry and boundary condition of biaxial test are shown in Fig. 6. Axial compression is applied to the specimen by vertical velocity (1.2mm/min) of the top nodes. A Drucker-Prager yield criterion and isotropic linear softening is used. The weak imperfection is introduced in the top right part of the specimen to trigger numerically a shear band. The imperfection has got the size of four elements. The initial apparent cohesion of this zone is assumed be equal to 60 percent of the apparent cohesion in other parts of the specimen. The material parameters used during the computations are Poisson's ratio υ= 0.4, solid grain density ρ_s =2000 kg/m^3, water density ρ_w=998.2 kg/m^3, Linear softening modulus H=-15MPa, solid grain bulk modulus K_s= 6.78 GPa, water bulk modulus K_w= 0.20 GPa. The Angle of internal friction and dilatancy are exactly the same as in Refs [30, 31]. Table 1 lists other parameters which are obtained by calibration. The parameter γ is set to 1cm and m is set to 1.5.

Fig. 7 shows the calculated normalized stress–strain curve in comparison with the experimentally obtained curves. The investigated range of confining pressure stress is 100–800KPa for dense RF Hostun sand. The calculated curves coincide very well. Only the nonlinearity of the initial stiffness is underestimated in the calculations. The stress drop after reaching the peak can also be seen in the calculation. It is apparent that when increasing the confining stress, the onset of strain localization is delayed, as observed for dense sand. Moreover, the peak value of stress ratio clearly depends on the confining stress. As in the laboratory tests, in the numerical simulation, the shear band starts from the top of the specimen. The development of shear band is shown by the contours of symmetric part of the acoustic tensor depicted in Figs 7. The onset of localization and the development of a complete localization inside the specimens are clearly revealed by the determinant of the symmetric part of the acoustic tensor. The pattern of the shear band is similar to what was observed in the laboratory tests [31]. The contours of symmetric part of the acoustic tensor indicated that shear banding initiates at, or shortly before peak. The stress drop is associated with the complete development of a shear band. Figure 8 presents the sequence of incremental effective plastic strain contours during a drained test on dense Hostun RF sand under 100KPa confining pressure. The calculated shear band inclination is determined from the distribution of the effective plastic strain (Figure 9). In the calculations the shear band thickness does not change with increasing confining pressure. In table 2, the numerically obtained shear band orientations are compared with the experimentally obtained shear band orientation. This is in accordance with the observations of Desrues and Viggiani [2] for biaxisal tests on different dense sands. The inclination of the shear zone increases with increasing mean stress level. Figure 10 presents the sequence of incremental displacement vectors during a drained test on dense Hostun RF sand under 100KPa confining pressure. Between axial displacement of 1.5 and 2 cm, the deformation clearly consists of nearly undeformed portions of the specimen sliding over each other. The effective plastic strain along a vertical (central) cross-section and for different deformations is shown in Fig 11. Maximum effective plastic strain value decreased as confining pressure stress increased.

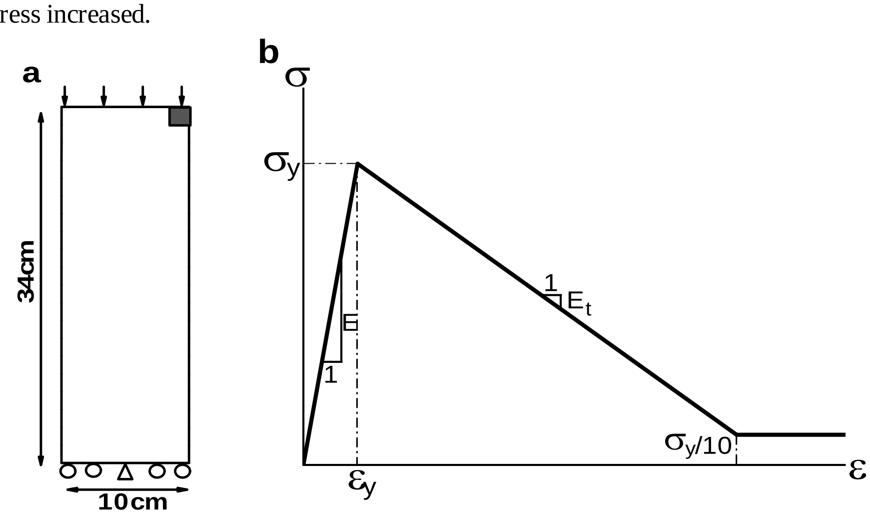

Fig.6 The biaxial specimen; (a) The geometry and boundary conditions, (b) the stress–strain curve

Table 1 Material parameters used in the computation

	σ_3'	Young modulus(E)	apparent cohesion (c_0)
drained test on dense sand	100KPa	2000 MPa	1 MPa
drained test on dense sand	200KPa	2500 MPa	2.5 MPa
drained test on dense sand	400KPa	2750 MPa	5 MPa
drained test on dense sand	800KPa	4000 MPa	8.5 MPa

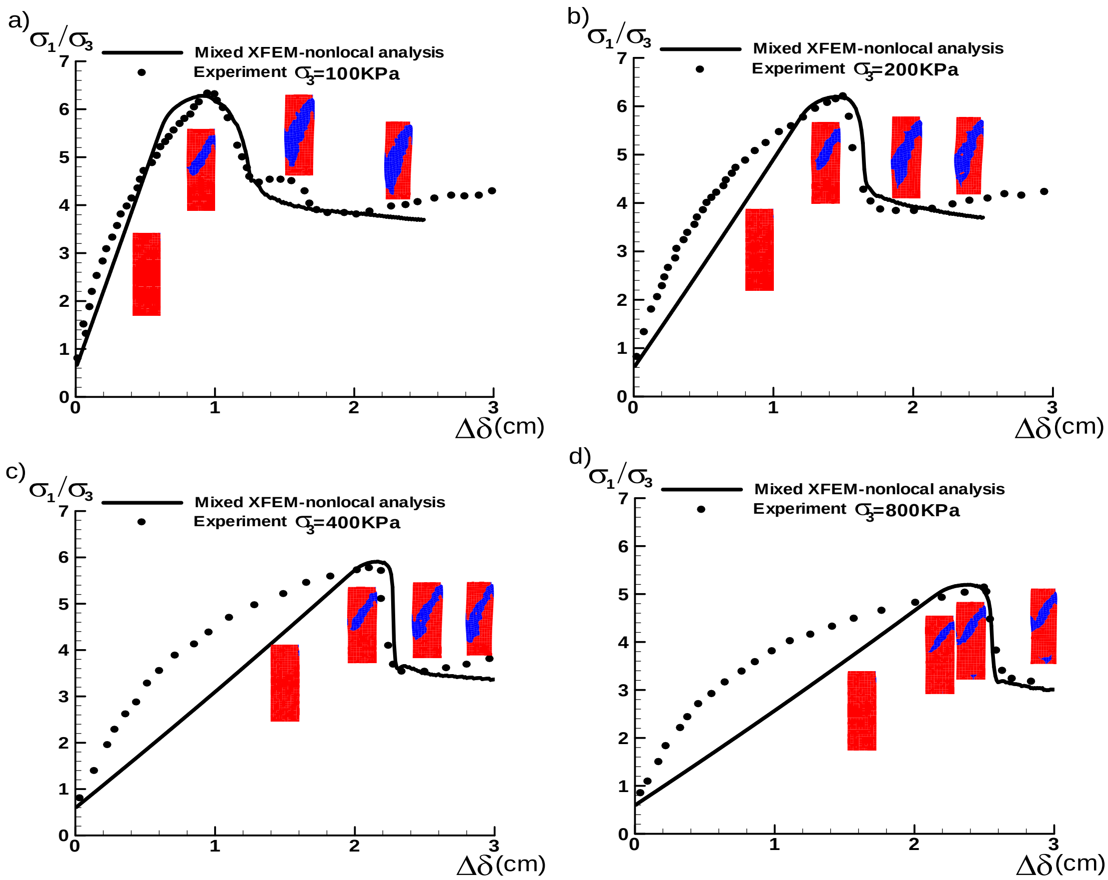

Fig.7 Experimental and numerical load-displacement curve and contours of symmetric part of the acoustic tensor for dense sand under (a) 100KPa (b) 200KPa (c) 400KPa (d) 800KPa confining pressure

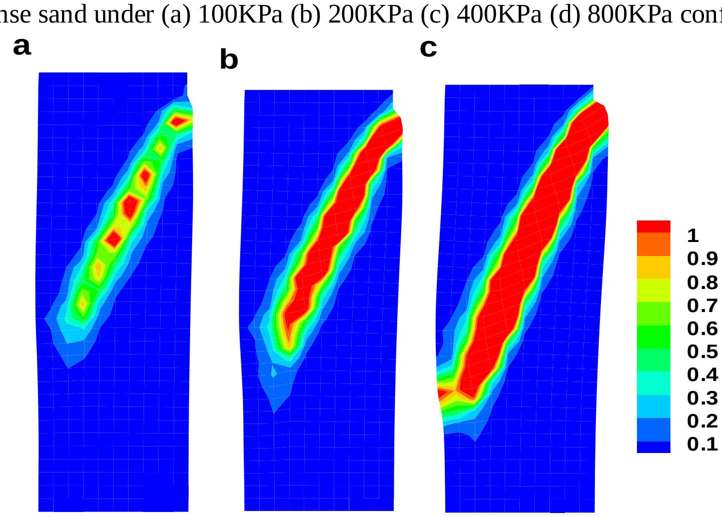

Fig.8 The effective plastic strain contours at different deformations for dense sand under 100KPa confining pressure; (a) Δδ=1.2cm (b) Δδ=1.5cm (c) Δδ=2cm

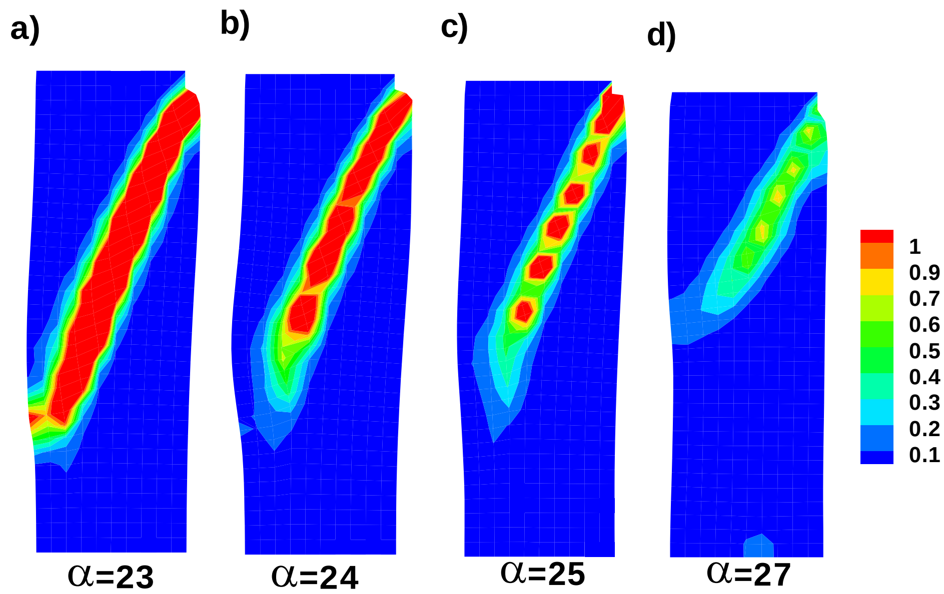

Fig.9 the effective plastic strain contour and orientation of the shear band for dense sand under (a) 100KPa (b) 200KPa (c) 400KPa (d) 800KPa confining pressure

Table 2 Numerically and experimentally obtained shear band orientation

σ'_3	numerically obtained orientation	experimentally obtained orientation [3]
100*KPa*	23	21
200*KPa*	24	24.5
400*KPa*	25	25.5
800*KPa*	30	30

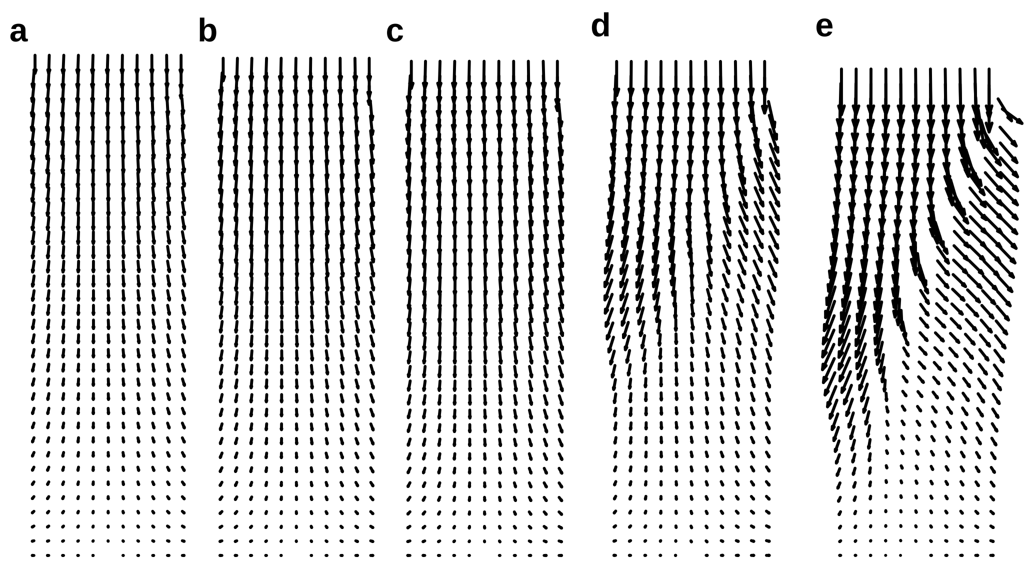

Fig.10 Incremental displacement vectors for dense sand under 100KPa confining pressure; (a) Δδ=.8cm (b) Δδ=1cm (c) Δδ=1.2cm (d) Δδ=1.5cm (e) Δδ=2cm

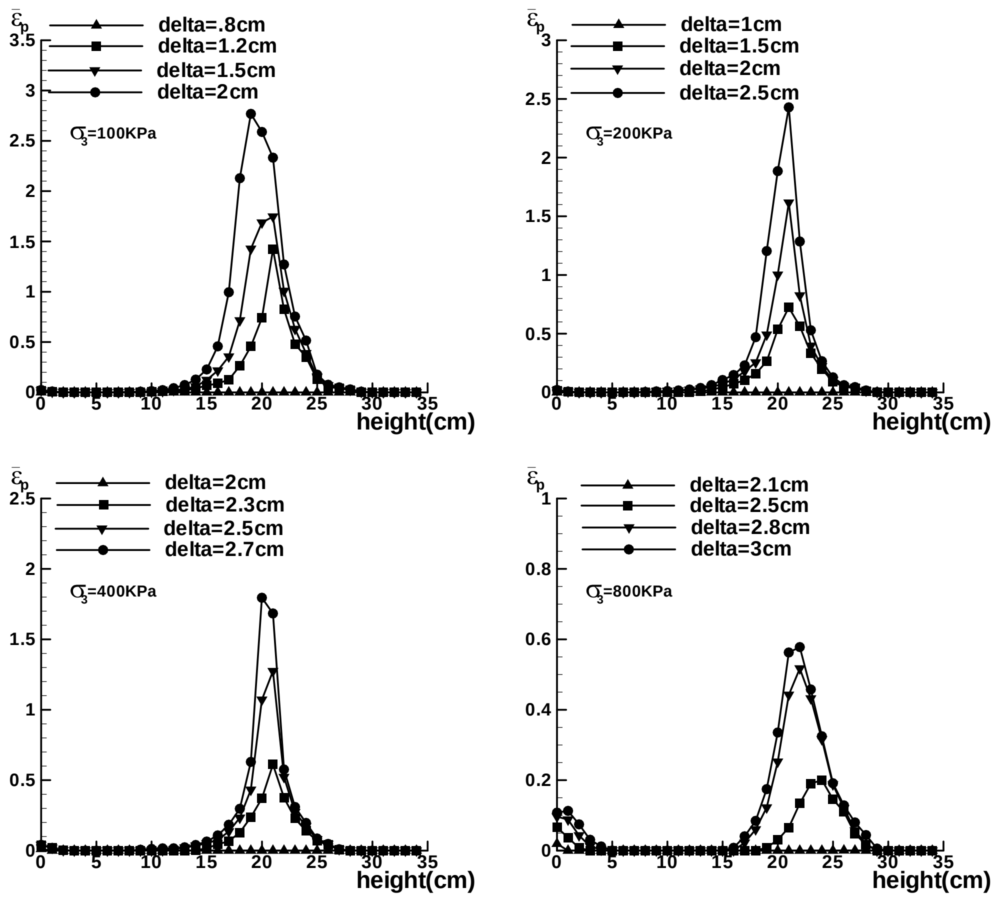

Fig.11 The effective plastic strain along a vertical cross section through the centre for dense sand under (a) 100KPa (b) 200KPa (c) 400KPa (d) 800KPa confining pressure

6. Conclusion

The integral type nonlocal model enhanced by XFEM method for granular materials like e.g. sands was presented by introducing a nonlocal plastic strain into the stress-strain relation. The numerical calculations of a plane strain compression test that the mesh dependence in classical continuum mechanics was remedied using the integral type nonlocal model enhanced by XFEM method. In section 2, The nonlocal model of Bazant and Lin [13] was extended. In section 3, governing equations were briefly recalled and XFEM was applied to the governing equations. Approximation of the displacement field in the localization band was improved by incorporating a set of special enrichments. The tangent stiffness matrix was derived for the mixed XFEM-integral type nonlocal formulation. Standard FE analysis was first employed with no enrichment functions to perform the numerical simulation. The enrichment functions were then incorporated into the standard shape functions after the evolution of the localization band.

In section 4, a new method based on the local bifurcation theory was proposed for the initiation and growth criterion of the strain localization interface. When using this method, the softening zone initiation locus did not need to be known in advance. In section 5-1, It was shown that the nonlocal model preserved the well-posedness of the governing equations in the post-localization regime and prevented pathological mesh sensitivity of the numerical results if the size of the element was smaller than $\gamma/2$. The mixed XFEM-nonlocal model guaranteed mesh independence even if the size of the elements was larger than $\gamma/2$. In the other words, coarser mesh can be used for XFEM combined with a nonlocal model than when using only a nonlocal model. The computational effort required for the mixed XFEM-nonlocal model was less than for the nonlocal formulation because coarser mesh can be used in simulation. In section 5-2, the ability of the proposed model to describe the behavior of granular materials was demonstrated by comparisons of the results of numerical calculations and biaxial tests on dense Hostun RF sand. The calculated stress-strain curve as well as the shear band inclination corresponded very well with the experimental results. The singularity of the symmetric part of the acoustic tensor was considered as the onset condition of strain localization. It was shown that, the initiation of the localization took place before the peak in the overall stress strain curve. The shear band was not simultaneously initiated at every point, but it propagated from an initiation point with a constant direction. Based on the results of the numerical simulation presented herein, the following conclusions can be drawn concerning drained compression of dense Hostun RF sand. 1- The onset of the localization in form of shear bands was significantly affected by the confining pressure level. The localization was retarded by increasing mean stress level. 2- The orientation of shear zones increased with increasing pressure level. 3- The peak value of stress ratio clearly depended on the confining stress.4- The use of the determinant of the symmetric part of the acoustic tensor allowed for representing the evolution of localized deformation 5- In the calculations the shear band thickness does not change with increasing confining pressure. 6- The numerical calculations shown that shear localization in granular bodies can be studied with the integral type nonlocal model enhanced by XFEM method.

Acknowledgment

The authors declare that they have no conflicts of interest in the research.

REFERENCES

1. de Borst, R., L.J. Sluys, H.B. Muhlhaus and J. Pamin, 1993. Fundamental issues in finite element analyses of localization of deformation. Engng. Comput., 10 (2): 99-121.

2. Sulem, J. and I. Vardoulakis, 1995. Bifurcation Analysis in Geomechanics. Blackie Academic and Professional Publishers, pp: 462.

3. Pijaudier-Cabot G. and Benallal A., 1993. Strain localization and bifurcation in a nonlocal continuum. Int. J. Solids Struct., 30 (13): 1761–1775.

4. Jirasek, M. and S. Rolshoven, 2003. Comparison of integral-type nonlocal plasticity models for strain softening materials. Int. J. Engng. Sci., 41 (13): 1553-1602.

5. Tejchman, J., 2002. Patterns of shear zones in granular materials within a polar hypoplastic continuum. Acta. Mech., 155 (1–2): 71–95.

6. de Borst, R. and HB. Muhlhaus, 1992. Gradient dependent plasticity: formulation and algorithmic aspects. Int. J. Numer. Meth. Engng., 35 (3): 521–539.

7. Loret, B. and J.H. Prevost, 1990. Dynamic strain localisation in elasto(visco-)plastic solids. Part 1. General formulation and one-dimensional examples. Comput. Meth. Appl. Mech. Engng., 83 (3): 247–273.

8. Tejchman, J., 2003. A non-local hypoplastic constitutive law to describe shear localisation in granular bodies. Arch. Hydro-Engineering Environ. Mech., 50 (4): 229–250.

9. Zarinfar, M. and F. Kalantary, 2013. Numerical simulation of strain localization using mixed XFEM-integral type nonlocal model. MEJSR, 16 (1): 73-87.

10. Eringen, A.C., 1981. On nonlocal plasticity. Int. J. Engng. Sci., 19 (12): 1461–1474.

11. Eringen, A.C., 1983. Theories of nonlocal plasticity. Int. J. Engng. Sci., 21 (7): 741–751.

12. Pijaudier-Cabot, G. and Z.P. Bazant, 1987. Nonlocal damage theory. J. Eng. Mech., 113 (10): 1512–1533.

13. Bazant, Z.P. and F.B. Lin, 1988. Nonlocal yield-limit degradation. Int. J. Numer. Meth. Engng., 26 (8): 1805–1823.

14. Stromberg, L. and M. Ristinmaa, 1996. FE-formulation of a nonlocal plasticity theory. Comput. Meth. Appl. Mech. Engng., 136 (1-2): 127-144.

15. Brunig, M., S. Ricci and H. Obrecht, 2001. Nonlocal large deformation and localization behavior in metals. Comput. Struct., 79 (22-25): 2063–2074.

16. Maier, T.h., 2003. Nonlocal modeling of softening in hypoplasticity. Comput. Geotech., 30 (7): 599-610.

17. Maier, T., 2004. Comparison of non-local and polar modelling of softening in hypoplasticity. Int. J. Numer. Anal. Meth. Geomech, 28 (3): 251–268.

18. Tejchman, J., 2004. Comparative FE-studies of shear localizations in granular bodies within a polar and non-local hypoplasticity. Mech. Res. Commun., 31 (3): 341–354.

19. Jirasek, M., 1998. Nonlocal models for damage and fracture comparison of approaches. Int. J. Solids Struct., 35 (31-32): 4133-4145.

20. Bazant, Z.P. and M. Jirasek, 2002. Nonlocal integral formulations of plasticity and damage survey of progress. J. Eng. Mech., 128 (11): 1119-1149.

21. Melenk, J.M. and I. Babuska, 1996. The Partition of Unity Finite Element Method: Basic Theory and Applications. Comput. Meth. Appl. Mech. Engng., 139 (1): 289-314.

22. Belytschko, T. and T. Black, 1999. Elastic crack growth in finite elements with minimal remeshing. Int. J. Numer. Meth. Engng., 45 (5): 601-620.

23. Fries, T.P. and T. Belytschko, 2010. The extended/generalized finite element method: an overview of the method and its applications. Int. J. Numer. Meth. Engng., 84 (3): 253–304.

24. Patzak, B. and M. Jirasek, 2003. Process zone resolution by extended finite elements. Eng. Fract. Mech., 70 (7): 957-977.

25. Samaniego, E. and T. Belytschko, 2005. Continuum–discontinuum modelling of shear bands. Int. J. Numer. Meth. Engng., 62 (13): 1857-1872.

26. Areias, P. M. A. and T. Belytschko, 2006. Two-scale shear band evolution by local partition of unity. Int. J. Numer. Meth. Engng., 66 (5): 878–910.

27. Song, J.H., P.M.A Areias and T. Belytschko, 2006. A method for dynamic crack and shear band propagation with phantom nodes. Int. J. Numer. Meth. Engng., 67 (6): 868-893.

28. Areias, P. M. A. and T. Belytschko, 2007. Two-scale method for shear bands: thermal effects and variable bandwidth. Int. J. Numer. Meth. Engng., 72 (6): 658–696.

29. Khoei, A.R. and K. Karimi, 2008. An enriched-FEM model for simulation of localization phenomenon in Cosserat continuum theory. Comput. Mater. Sci., 44 (2): 733–749.

30. Desrues J. and Hammad W., 1989. Shear banding dependency on mean stress level in sand In the Proceedings of the International Workshop on numerical methods for localization and bifurcation of granular bodies, pp: 25-30

31. Desrues J. and Viggiani G., 2004. Strain localization in sand: an overview of the experimental results obtained in Grenoble using stereophotogrammetry. Int. J. Numer. Anal. Meth. Geomech., 28: 279–321.

32. Bigoni, D. and T. Hueckel, 1991. Uniqueness and localization - I: associative and nonassociative elastoplasticity. Int. J. Solids Struct., 28 (2): 197-213.

33. Hill, R., 1962. Acceleration waves in solids. J. Mech. Phys. Solids., 10 (1): 1-16.

34. Rice, J.R., 1976. The localization of plastic deformation. In the Proceedings of the Theoretical and Applied Mechanics, pp: 207-220

35. Benallal, A. and C. Comi, 2003. Perturbation growth and localization in fluid saturated inelastic porous media under quasi-static loadings. J. Mech. Phys. Solids, 51 (5): 851–899.

36. Bésuelle, P. and R. Chambon, 2006. Modelling the post-localization regime with local second gradient models non uniqueness of solutions and non persistent shear bands. In the Proceedings of the Modern Trends in Geomechanics, pp: 209-221

37. Andrade, J.E. and R.I. Borja, 2007. Modeling deformation banding in dense and loose fluid saturated sands. Finite Elem. Anal. Des., 43 (5): 361–383.